Sensors & Actuators: B. Chemical 466 (2026) 140232

Contents lists available at ScienceDirect

Sensors and Actuators: B. Chemical

journal homepage: www.elsevier.com/locate/snb

Establishing label-free quantitative X-ray dose-response profiling by holo-tomographic flow cytometry

Daniele Pirone [a], Chiara de Vita [b], Rocco Mottareale [b], Giusy Giugliano [a,c], Gennaro Giordano [a], Simonetta Grilli [a], Vittorio Bianco [a], Lisa Miccio [a,*], Pasquale Memmolo [a], Marco Durante [b,d,e], Mariagabriella Pugliese [b,*], Pietro Ferraro [a]

[a] CNR-ISASI, Institute of Applied Sciences and Intelligent Systems "E. Caianiello", Via Campi Flegrei 34, Napoli, Pozzuoli 80078, Italy
[b] Department of Physics "E. Pancini", University of Naples "Federico II", Via Cinthia, Naples 80126, Italy
[c] Department of Mathematics and Physics, University of Campania "Luigi Vanvitelli", Viale Abramo Lincoln 5, Caserta 81100, Italy
[d] GSI Helmholtzzentrum für Schwerionenforschung, Biophysics Department, Darmstadt, Germany
[e] Department of Physics, Institute of Condensed Matter Physics, Technische Universität Darmstadt, Darmstadt, Germany

ARTICLE INFO

Keywords:
Quantitative phase imaging
Holographic tomography in flow cytometry
Label-free biosensing
Single-cell biophysical markers
Radiobiology
X-ray dose-response
Radiotherapy

ABSTRACT

Flow cytometry (FC) offers multiparametric analysis capabilities that can quantify cellular damage after exposure to cytotoxic agents. Here, we present a comprehensive study establishing a label-free quantitative X-ray dose-response profiling using a novel FC modality based on 3D Quantitative Phase Imaging, termed Holo-Tomographic Flow Cytometry (HTFC). This approach enables fully label-free 3D refractive index (RI) measurements, allowing detailed and quantitative characterization of the biophysical properties and morphology of living cells exposed to X-rays. By analyzing datasets of 3D RI tomograms from cells irradiated at graded doses, we identify intracellular biophysical markers that define a robust X-ray dose-response curve. Validation against standard clonogenic survival assays on three model cancer cell lines reveal a high correlation (>90%). HTFC not only eliminates labeling and operator bias but also markedly reduces experimental time from 1 to 2 weeks to 24 h, offering a fully automated and objective readout. While clonogenic survival remains the benchmark for radiosensitivity assessment, our findings establish HTFC as a powerful label-free platform for fast assessment of radiation damage. This technology paves the way for predictive biosensors that can capture patient-specific responses, thereby supporting the transition from conventional, uniform radiotherapy protocols to personalized treatment strategies.

1. Introduction

Cell populations are inherently heterogeneous in morphology, size, cell cycle phase, and physiological state [1]. For this reason, the detailed characterization of individual cells has become a major objective in contemporary biomedicine and personalized medicine, which increasingly rely on advanced cytometric platforms for the single-cell analysis [2]. A significant advancement in cytometric analysis has been the integration of Flow Cytometry (FC) [3] with microscopy, leading to Imaging Flow Cytometry (IFC). Over the past decades, IFC has enabled substantial progress in cell biology studies [4], rapidly establishing itself as a reference method in diverse biomedical fields, including cancer research [5]. IFC simultaneously records bright-field, dark-field, and fluorescence images from individual cells as they move in a microfluidic stream, thus providing a high-throughput acquisition of spatially resolved data. The resulting large datasets allow extraction of multiple morphological and functional parameters at the single-cell level. Among its emerging applications, IFC has recently shown great promise in biodosimetry [6–8], a field devoted to quantifying biological responses to ionizing radiation for the estimation of absorbed doses and evaluation of radiation-induced cellular damage [9]. For example, IFC has been applied to evaluate radiation response in lymphocytes from umbilical cord blood and cancer patients [10] or to enable high-throughput quantification of DNA double-strand break repair kinetics through γ-H2AX analysis [11]. Despite its significant advantages, IFC still faces several drawbacks that limit its broader adoption in biomedical research. The technique remains inherently fluorescence-dependent, operator-sensitive, and often time-consuming and costly. It requires

* Corresponding authors.
E-mail addresses: daniele.pirone@isasi.cnr.it (D. Pirone), lisa.miccio@isasi.cnr.it (L. Miccio), mgpuglie@unina.it (M. Pugliese).

https://doi.org/10.1016/j.snb.2026.140232
Received 19 January 2026; Received in revised form 4 May 2026; Accepted 21 May 2026
Available online 26 May 2026

prior knowledge of appropriate exogenous markers, which can affect measurement accuracy due to photobleaching and may introduce phototoxic effects that alter cellular physiology. Once labeled, cells cannot be reused for downstream analyses. Most critically, IFC provides limited access to the intrinsic biophysical properties of cells, as it primarily captures morphological and fluorescence intensity features rather than quantitative physical information. Therefore, label-free approaches have recently attracted growing interest, as they allow the study of cellular processes without relying on exogenous dyes. For instance, direct mass spectrometry has been applied to investigate bystander effects in chondrocytes co-cultured with chondrosarcoma cells irradiated with X-rays or carbon ions [12], Raman micro-spectroscopy has been used to assess the impact of X-ray irradiation on nuclear and membrane regions of single neuroblastoma cells [13], and, more recently, lab-on-a-chip impedance spectroscopy has been employed to monitor radiotherapy responses even in 3D spheroids [14]. Among label-free microscopy methods [15], Quantitative Phase Imaging (QPI) has emerged as a particularly powerful tool over the past decades [16]. Typically, QPI exploits the interferometric properties of Digital Holography (DH) to reconstruct Quantitative Phase Maps (QPMs) of individual cells [17,18]. In a QPM, both cell morphology and the spatial distribution of the refractive index (RI) are encoded in a 2D image. Thus, unlike fluorescence images, QPMs provide more distinctive information on the cellular state [19], since the RI is a fundamental biophysical parameter [20,21]. DH has been proposed as a label-free approach for the non-invasive, quantitative assessment of the morphological changes of γ-irradiated human mesenchymal stem cells and periosteal cells [22], X-irradiated breast cancer cells [23], and X-irradiated urothelial bladder carcinoma cells [24]. Moreover, combined to FC, we have recently demonstrated that DH can measure the effects of X-ray radiations on single flowing lymphocytes and classify the irradiation dose by machine learning tools [25]. The most recent advancement in label-free bioimaging is the 3D extension of QPI, known as Holographic Tomography (HT), which opens unprecedented opportunities by providing access to the full RI volumetric distribution of single cells [26]. Among the various HT configurations [27,28], we have developed Holo-Tomographic Flow Cytometry (HTFC), which integrates the label-free, quantitative, and 3D capabilities of HT with single-cell analysis. Conversely to well-established and traditional IFC, HTFC acquires multiple images for each cell while undergoing rotation in microfluidic environment. Advanced numerical processing of multiple cell perspectives provides 3D tomographic images of each cell flowing and rotating into the Field-of-View exploiting the inner RI contrast of the cellular sub-compartments. Consequently HTFC is an high content imaging modality supplying 3D morphological and structural information. Furthermore such informative content is quantitatively related to the biophysical properties of the cell and not on the intensities of the fluorescence tags. IFC main benefits are the high throughput and specificity. HTFC operate at a lower throughput compared with IFC while providing 3D phase-contrast and morphological features not accessible by IFC. The main advantage of HTFC is its completely stain-free nature that prevents all the fluorescence correlated drawbacks. Furthermore it has been recently demonstrated that HTFC can provide specificity identifying some cellular inner structures as nucleus, lysosomes, lipid droplets and vacuoles [29–35].

Here, by exploiting the unique capabilities of HTFC, we present for the first time a label-free quantitative X-ray dose-response profiling obtained using a 3D QPI technique. Thus, we correlate 3D biophysical markers with cancer cell responses to defined X-ray irradiation strategies and their effectiveness. In the FC configuration, we acquire comprehensive datasets of 3D RI tomograms from single cells exposed to different X-ray irradiation doses. An *ad hoc* statistical segmentation algorithm [31] is then applied to extract nucleus-specific information from stain-free, quasi-spherical cells, thereby faithfully reproducing the intracellular organization under suspension conditions. For each dose, we derive quantitative single-cell biomarkers, which enable us to evaluate the effects of X-ray irradiation across the entire cell population and, ultimately, to construct a label-free dose-response curve. We demonstrated in a previous work that label-free 2D QPI measurements can classify irradiation doses and capture their effects on living cells [25]. Starting from that preliminary result, here we validate HTFC as a sensing platform able to detect distinctive signatures of radiosensitivity on three different model-cancer cell lines after 24 h from irradiation in the range between 0,25 Gy and 2 Gy by analysing single cells at a throughput of hundreds of cell per minute. We compare HTFC biosensor readouts with state-of-art biodosimetry measurements by performing clonogenic assays on the same model-cancer cell lines observing a strong correlation (>90%) between the two approaches. HTFC biosensor allows to obtain a dose-response curve in a drastically reduced time compared to clonogenic assay outputs that require 1–2 weeks. The results demonstrate the proof-of-concept that HTFC can be established as a label-free biosensor [36] capable of predicting tumor responses to ionizing radiation in a rapid, automatic, and objective manner. This approach could open new routes on personalization of radiotherapy (RT) treatments, which remain a cornerstone of multidisciplinary cancer care [37]. In fact, current RT protocols still rely on a one-size-fits-all principle, yet it is well recognized the importance for tailoring treatment to individual patient characteristics and selecting the most appropriate RT protocol as patient responses to radiation vary widely [38].

2. Material and methods

2.1. Sample preparation

Neuroblastoma SHSY5Y and SKNBE2 cells, as well as breast cancer MCF7 cells, were cultured in Falcon® T25 flasks under standard conditions. SHSY5Y cells were maintained in Dulbecco's Modified Eagle Medium (DMEM, Avantor, VWR) supplemented with 20% fetal bovine serum (FBS, Avantor, VWR), 1% penicillin-streptomycin (P/S, biowest), and 1% L-glutamine (Sigma, St. Louis, MO, USA). SKNBE2 cells were cultured in a 1:1 mixture of DMEM and Ham's F-12 nutrient mixture (Ham's F12, Avantor, VWR) supplemented with 10% FBS, 1% P/S, and 1% L-glutamine. MCF7 cells were maintained in DMEM supplemented with 10% FBS, 1% P/S.

All the samples for all the cell lines were prepared at a concentration of $\geq$ 300,000 cells/ml to meet HTFC experimental requirements. Cell vitality and proliferation were monitored daily using the LUNA-II™ Automated Brightfield Cell Counter. Cultures were incubated at 37 °C in a humidified atmosphere containing 5% CO_2. The cell concentrations for the clonogenic assay varied on the doses.

2.2. Irradiation experiments

Neuroblastoma SHSY5Y cells, neuroblastoma SKNBE2 cells, and breast cancer MCF7 cells were exposed to X-rays administered through conventional external beam radiotherapy at the IRCCS Istituto Nazionale Tumori Fondazione Pascale in Naples (Italy). The irradiation of samples was conducted using the Versa HD clinical LINAC system by ELEKTA, which utilizes a 6 MV electron beam to generate X-rays. Different radiation doses were delivered to the cell cultures using 3D conformal radiotherapy (3D-CRT). In particular, 0.5 Gy, 1 Gy, 2 Gy, and 4 Gy were used with SHSY5Y cells, while 0.25 Gy, 0.5 Gy, 1 Gy, 1.5 Gy, and 2 Gy were used with SKNBE2 and MCF7 cells. The 3D-CRT treatment plans were developed with Elekta's Monaco v5.11.03 treatment planning system (TPS), which combines Monte Carlo dose calculation accuracy with robust optimization tools to deliver high-quality radiotherapy treatment. Falcon® T25 cell culture flasks were placed in a uniform 20 × 20 cm^2 square field and positioned between two plexiglass plates (ScandiDos Delta-4 Calibration Phantom): the first plate (3 cm thick) was used to simulate the dose buildup effect for shallow penetration depths, while the second plate (5 cm thick) was included to stop

backscattered radiation. The cell samples were irradiated from opposing fields via a 180° gantry rotation, delivering X-rays at a fixed dose rate of 200 monitor units (MU) per minute. This experimental setup allowed for the uniform administration of the prescribed doses at the cellular level. Following clinical radiotherapy exposure, the cells were stored in an incubator at 37°C in a 5% CO2 atmosphere, in preparation for subsequent HTFC analyses (24 h post-irradiation) and clonogenic survival assays (1–2 weeks post-irradiation).

2.3. Clonogenic assay

The clonogenic assay, the gold standard for measuring cellular radiosensitivity, was used to assess radiation-induced cell death [39]. The assay defines a cell as surviving irradiation if it retains its

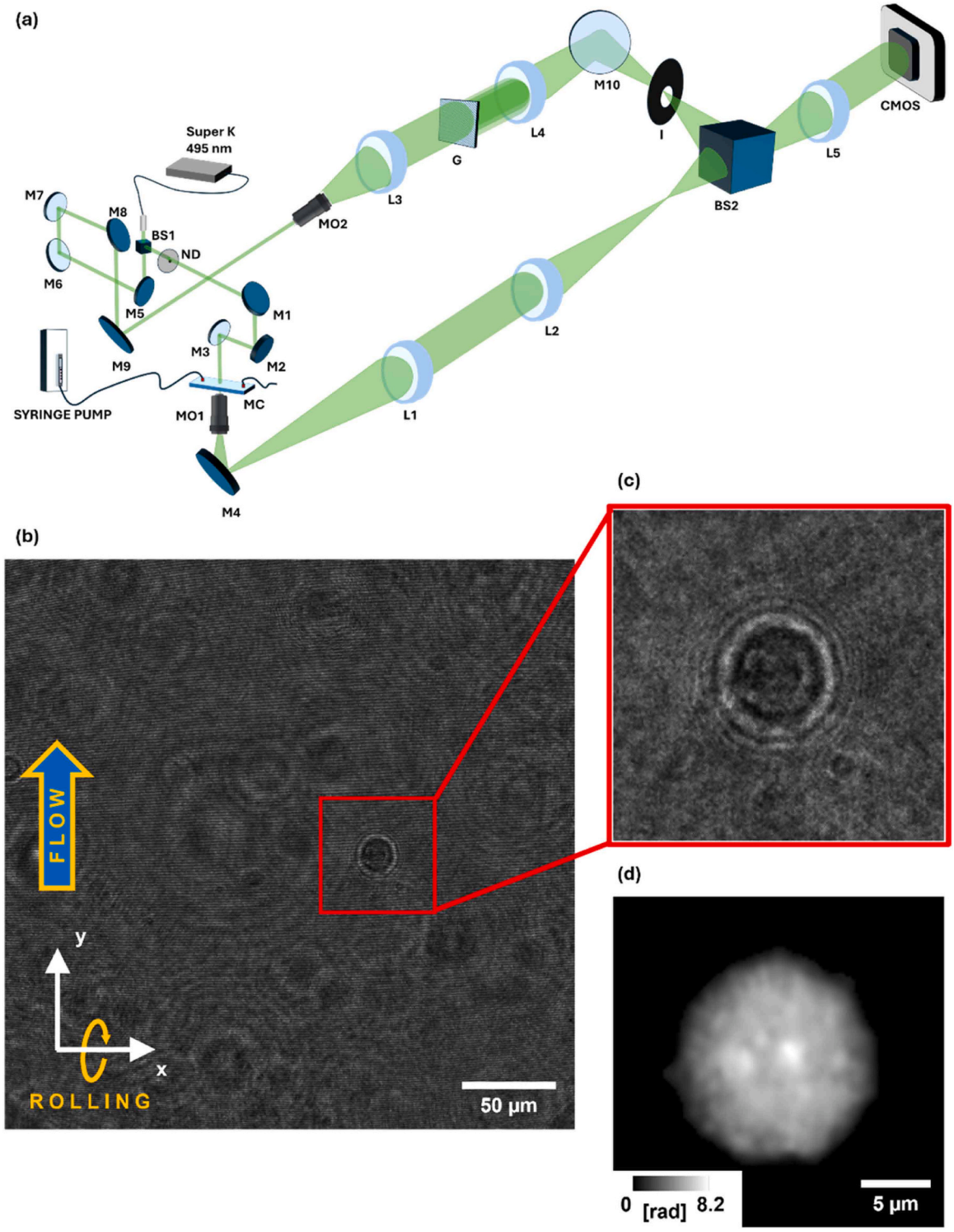

Fig. 1. HTFC experimental system and numerical reconstruction. (a) Sketch of the opto-fluidic recording system. SuperK, laser-light source; BS, beam splitters; ND, neutral density filter; M, mirrors; MO, microscope objectives; L, lenses; G, diffraction grating; I, iris diaphragm. (b) Hologram taken from a recorded video sequence of control neuroblastoma SKNBE2 cells. (c) Sub-hologram highlighted in (b). (d) QPM reconstructed from the sub-hologram in (c).

proliferative potential and forms a colony of at least 50 cells. Cells were seeded at different densities the day before the irradiation, with the concentration optimized according to the radiation dose. Specifically, the number of seeded cells depends on the dose the cells will be exposed to. Such number is estimated based on the α and β coefficients of the clonogenic assay present in the literature and the Plating Efficiency (PE) of the cell line. The PE was estimated before the experiment, seeding a number of cells and counting the colony formed after the time required for colonies to form. In this experiment, the number of cells seeded are: 500 cells for 0 Gy; 550 cells for 0.25 Gy; 600 cells for 0.5 Gy; 700 cells for 1 Gy; 800 cells for 1.5 Gy; 1000 cells for 2 Gy. For each cell line analyzed, three replicates (T25 flasks) were seeded for each dose, including the non-irradiated sample (0 Gy). Following exposure, the flasks were returned to the incubator. After 1–2 weeks of incubation (9 days for neuroblastoma SKNBE2 cells, 14 days for breast cancer MCF7 cells, and 14 days for neuroblastoma SHSY5Y cells), the samples were fixed and stained for manual counting. The points for the surviving curve are obtained as the average number of colonies of the triplicate. The surviving fraction SF for a given dose D was calculated as

$$SF(D) = \frac{number\ of\ colonies\ formed}{number\ of\ cells\ seeded \quad \times \quad plating\ efficiency}, \tag{1}$$

where the plating efficiency PE was calculated as

$$PE = \frac{number\ of\ colonies\ formed\ in\ control}{number\ of\ cells\ seeded\ in\ control}. \tag{2}$$

The SF data were finally fitted using an LQ model, i.e. McMahon [40]

$$SF(D) = e^{-\alpha D - \beta D^2}, \tag{3}$$

as also shown in Fig. S1.

2.4. HTFC experiments

Hologram acquisition was carried out using a Mach–Zehnder interferometer with symmetric optical paths [29], as illustrated in Fig. 1(a). A collimated light source (SuperK FIANIUM, 495 nm, FWHM ≈ 4 nm) was split by beam splitter BS1 into an object and a reference beam. The object beam interacts with cells flowing through a microfluidic channel (PMMA, 1000 ×200 μm^2), and is collected by a microscope objective (MO1, Zeiss 63 ×/0.95 numerical aperture), followed by a tube lens L1 (150 mm focal length) and a telescope system composed of lenses L2 (150 mm focal length) and L5 (200 mm focal length). The reference beam travels along a separate optical path containing equivalent components: a microscope objective (MO2, Zeiss 63X/1.3 numerical aperture, dry) and tube lens L3 (150 mm focal length), followed by a second telescope with lenses L4 (150 mm focal length) and L5. The two beams are recombined at a second beam splitter (BS2). Temporal coherence is maintained using delay lines implemented with mirrors M1, M2 and M6, M7 in the object and reference arms, respectively. Spatial coherence is ensured by introducing a diffraction grating (Newport Moiré Grating, 80 lp/mm) in the reference arm and an iris diaphragm (I) to select only the first diffraction order. This choice assures homogeneity of the interference fringes across the whole field of view. The resulting off-axis interference pattern is captured by a CMOS camera (Genie Nano-CXP, 5120 ×5120, 4.5 μm pixel size).

To acquire multiple views of individual cells, hydrodynamic rotation was induced by positioning cells off-center in the microfluidic channel while maintaining a controlled flow rate of 75 nL/s using a CETONI neMESYS 290 N syringe pump [29–35]. According to the reference system in Fig. 1(b), cells flow along the y-axis and rotate around the x-axis. From each hologram of the recorded video sequence (5120 ×5120 corresponding to 305 ×305 μm^2), cells were tracked to extract squared sub-holograms containing each rotating cell (1024 ×1024 corresponding to 61 ×61 μm^2), as shown in Fig. 1(b). For each sub-hologram (see Fig. 1(c)), the real diffraction order was isolated via band-pass Fourier filtering exploiting the off-axis configuration [18]. The Angular Spectrum propagation method [18] was used to determine the optimal focus distance for each cell, minimizing the Tamura coefficient [41]. Phase-contrast images were obtained from the argument of the in-focus complex field, followed by phase aberration correction through subtraction of a reference hologram [42] and phase denoising based on the windowed Fourier transform filter [43]. Finally, phase unwrapping based on the PUMA algorithm [44] was applied to generate QPMs for each sub-hologram (201 ×201 corresponding to 24 ×24 μm^2), as displayed in Fig. 1(d). For each cell, the stack of QPMs containing its rotation was employed to estimate the unknown rolling angles [45], and, finally, its 3D RI tomogram was reconstructed using the Filtered Back Projection algorithm [31–35,46], as reported in Fig. 2(a). All HTFC data to create label-free dose-response curves were obtained from a single independent experiment per dose, according to the numbers reported in Table S1, Table S3, and Table S5.

2.4.1. Fisher discriminant ratio calculation

To quantify differences among cell populations, we computed the distance of each irradiated cluster from the control cluster in the 2D Principal Component Analysis (PCA) space using the Fisher Discriminant Ratio (FDR) [47]. Let $\bar{\bar{X}}_0$ and $\bar{\bar{X}}_D$ be the PCA matrix of the control population and the population irradiated by a certain dose D, respectively, where the PCA matrix contains the PCA features of all single cells of that population. Thus, $\bar{\bar{X}}_0$ and $\bar{\bar{X}}_D$ have size $N_0 \times d$ and $N_D \times d$, respectively, with d being the dimensionality of the PCA (i.e., 2 in this study), and N_0 and N_D being the number of cells in the control population and irradiated population, respectively. We computed the FDR at a certain dose D as

$$FDR_D = \bar{\delta}^T \bar{\bar{A}}\, \bar{\delta}, \tag{5}$$

with

$$\bar{\delta} = \bar{\mu}_D - \bar{\mu}_0 \tag{5}$$

and

$$\bar{\bar{A}} = \bar{\bar{\Sigma}}^{-1}, \tag{6}$$

where $\bar{\mu}_0$ and $\bar{\mu}_D$ respectively are the mean vectors of $\bar{\bar{X}}_0$ and $\bar{\bar{X}}_D$ across single cells (size d × 1), and $\bar{\bar{\Sigma}}$ is the total covariance matrix given by the sum of the control covariance matrix $\bar{\bar{\Sigma}}_0$ and the irradiated covariance matrix $\bar{\bar{\Sigma}}_D$.

Moreover, to estimate the uncertainty associated with the FDR_D between the multivariate control and irradiated populations, we used analytical error propagation based on a first-order Taylor expansion (also known as Gaussian error propagation) [48]. This method approximates the variance of a function of random variables based on the variances and covariances of its inputs. To propagate the uncertainty in FDR_D, we consider the uncertainty in the mean vector $\bar{\delta}$ by calculating its covariance matrix as

$$\bar{\bar{\Sigma}}_{\bar{\delta}} = \frac{1}{N_0}\bar{\bar{\Sigma}}_0 + \frac{1}{N_D}\bar{\bar{\Sigma}}_D \quad . \tag{7}$$

At this stage, we assume to neglect the uncertainty in the covariance matrices $\bar{\bar{\Sigma}}_0$, $\bar{\bar{\Sigma}}_D$, and then $\bar{\bar{\Sigma}}_{\bar{\delta}}$. This allows us to treat $\bar{\bar{A}}$ as a constant with respect to the uncertainty propagation. While this introduces a simplification, it enables a tractable analytical expression and remains a reasonable approximation when the number of samples is sufficiently large. Under this assumption, the uncertainty of FDR_D is

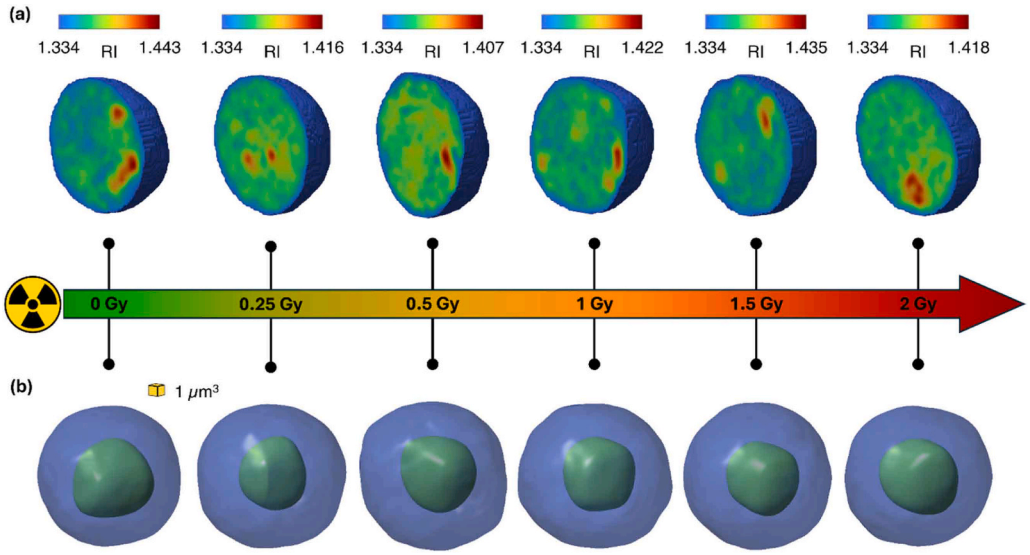

Fig. 2. HTFC reconstructions of different neuroblastoma SKNBE2 cells 24 h after the exposure to different X-ray irradiation doses. (a) Central slice of the 3D RI tomograms. (b) Isolevels representation of the 3D RI distribution in (a), with the CSSI-segmented nucleus (green) within the cytoplasm (blue).

$$\sigma_{FDR_D} = 2\sqrt{\bar{\delta}^T A \, \Sigma_{\bar{\delta}} A \, \bar{\delta}}\,. \tag{8}$$

This expression provides a first-order estimate of the uncertainty in the FDR_D distance due solely to the variability in the sample means. It is valid under the assumption that the sample means are approximately normally distributed, which is held asymptotically by the Central Limit Theorem. The FDR_D distances of the neuroblastoma SKNBE2 population are reported in Table S2 along with their uncertainties σ_{FDR_D}.

3. Results and discussion

3.1. Extraction of 3D biophysical markers to characterize the HTFC dataset at different X-ray irradiation doses

Using the HTFC experimental system, the neuroblastoma SKNBE2 cell line was analysed 24 h after X-ray irradiation at different doses. The primary objective was to investigate the cellular response to a heterogeneous spectrum of X-ray exposures under the following conditions: low doses (0.25 and 0.5 Gy), intermediate doses (1 and 1.5 Gy), and the standard fractionated dose typically used in clinical radiotherapy (2 Gy). For each cell, the corresponding 3D RI tomogram was reconstructed, yielding the dataset summarized in Table S1 corresponding to 590 SKNBE2 cells. The typical HTFC reconstructions obtained for different SKNBE2 cells 24 h after the exposure to 6 different X-ray irradiation doses, from 0 Gy up to 2 Gy, are shown in Fig. 2. In particular, Fig. 2(a) shows the representative central RI slices of the irradiated cells.

In label-free techniques such as QPI, the main limitation is the lack of intracellular specificity, since no marker is available to distinguish organelles from their background. Typically, intracellular RI contrast alone is insufficient to clearly differentiate subcellular structures [49]. To address this issue, advanced computational strategies have recently been developed to enhance intracellular specificity [50], including virtual staining methods based on deep learning [51]. In the case of HTFC, this challenge is even greater due to the suspended condition of single cells. To overcome it, we have previously demonstrated a Computational Segmentation based on Statistical Inference (CSSI) approach [31,34], which identifies organelles by exploiting the statistical similarity among voxels within their 3D RI volume. Since it is well established that ionizing radiation affects nuclear morphology [52], we applied the CSSI algorithm to segment the nucleus in the 3D RI tomograms of each SKNBE2 cell. Examples of segmented nuclei are reported in Fig. 2(b).

Building on the retrieved nuclear information, we carried out a multiplexed quantitative characterization at the single-cell level by extracting 39 biophysical markers related to the whole cell, nucleus, and cytoplasm (summarized in Table S7). For each compartment, we calculated seven features: RI mean, RI standard deviation, RI coefficient of variation, RI maximum, RI interquartile range, volume, and dry mass. The RI coefficient of variation was defined as the ratio between the RI standard deviation and the RI mean, while the dry mass represents the mass of the object excluding its aqueous content [16]. For each of these seven features, we also calculated the ratio between nuclear and cytoplasmic values. Moreover, for both the whole cell and the nucleus, we evaluated three morphological descriptors: sphericity, solidity, and extent. Sphericity was defined as the ratio of the surface area of a sphere with the same volume to the object's surface area, solidity as the ratio between the object's volume and the volume of its convex hull, and extent as the ratio between the object's volume and the volume of its bounding box. For each of these three descriptors, we additionally computed the ratio between nuclear and whole-cell values. Finally, we introduced two nucleus-to-cell features: the nucleus–cell normalized distance, defined as the Euclidean distance between the centroids of the nucleus and the cell normalized to the equivalent cell radius (i.e., the radius of a sphere with the same volume as the cell), and the nucleus–cell normalized solid angle, defined as the solid angle subtended by the nucleus from the cell centroid, normalized to 4π.

We ranked the 39 biophysical markers according to their ability to discriminate among the different irradiation doses using the ReliefF algorithm with 10 nearest neighbors [53]. As shown in the ranking reported in Fig. 3(a), the RI statistics of the various intracellular compartments (cell, nucleus, and cytoplasm) emerged as the most informative features, followed by their morphological features (i.e., sphericity, solidity, extent, and volume). This highlights the robustness of the selected feature set, which combines morphological descriptors (size and shape) with RI-based biomarkers calculated at both the whole-cell and intracellular levels, providing a meaningful characterization of the HTFC dataset across irradiation conditions. In Fig. 3(b), boxplots and corresponding one-sided violin plots are presented for some of the highest-ranked features. However, all the selected features display an oscillatory behavior across the irradiation doses compared to the control condition, indicating that none of them individually shows a monotonic trend suitable to serve as a reliable dose–response indicator. For instance, the cell RI maximum (1st) decreases from 0 Gy to 1.5 Gy

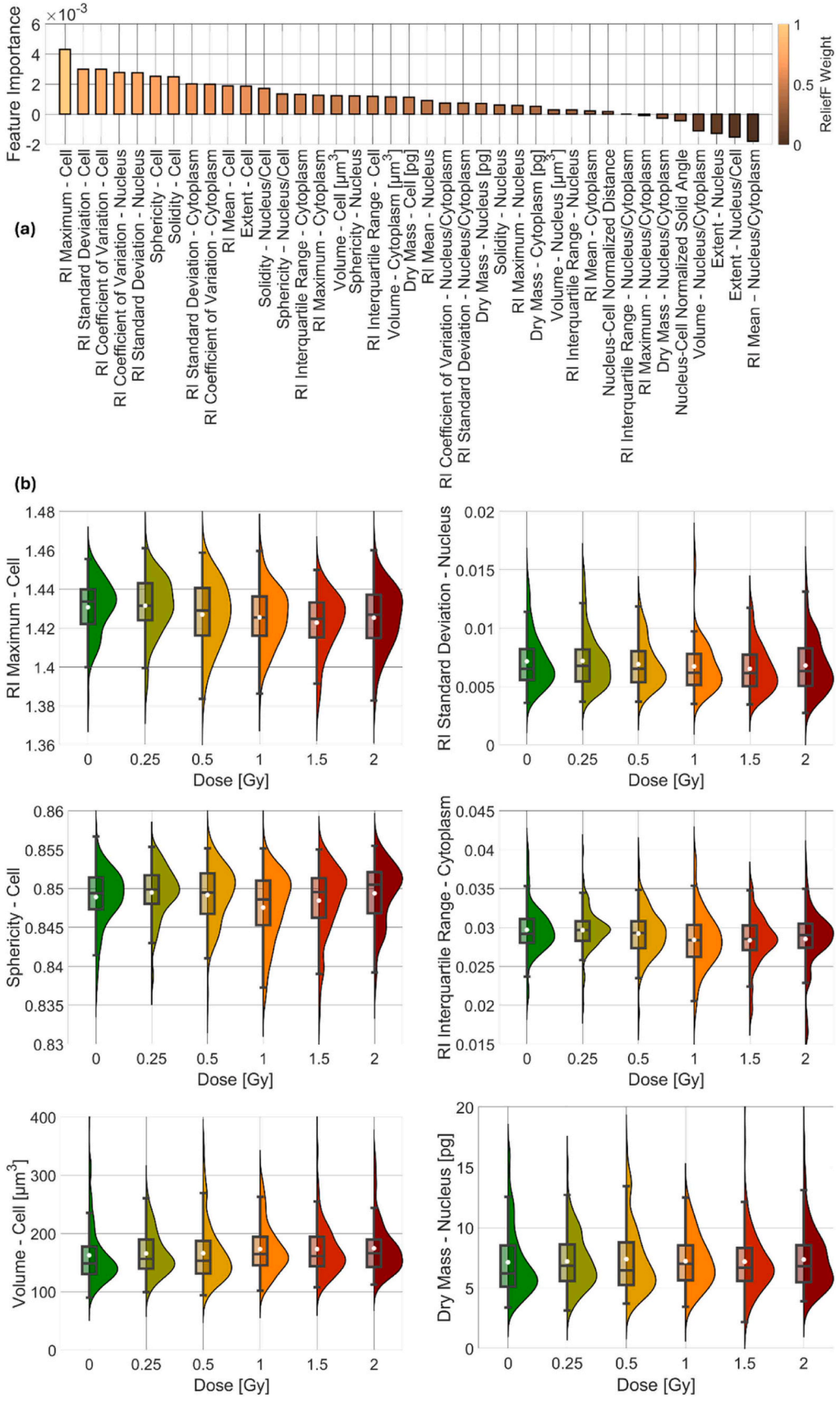

(caption on next page)

Fig. 3. Biophysical markers used to characterize the HTFC dataset of neuroblastoma SKNBE2 cells 24 h after exposure to different X-ray irradiation doses. (a) Feature ranking based on the ReliefF weights. (b) Boxplots and corresponding one-sided violin plots related to some of the highest-ranked features in (a). In each box, the white dot represents the mean value, the line inside represents the median, the lower and upper box limits correspond to the first and third quartiles, and the whiskers extend to the furthest values within the non-outlier range. The number of analysed cells for each dose was as follows: 0 Gy (n = 109), 0.25 Gy (n = 127), 0.5 Gy (n = 83), 1 Gy (n = 87), 1.5 Gy (n = 87), and 2 Gy (n = 97). All HTFC data were obtained from a single independent experiment per dose.

and then increases again at 2 Gy; the nucleus RI standard deviation (5th), cell sphericity (6th), and cytoplasm RI interquartile range (14th) increase at 0.25 Gy, decrease at 0.5 Gy and 1 Gy, and rise again at 1.5 Gy and 2 Gy; the cell volume (16th) and nucleus dry mass (24th) exhibit alternating oscillations across the dose range.

3.2. Definition of a label-free quantitative X-ray dose-response curve

We analysed the HTFC multiparametric redout by means of a PCA using all 39 biophysical markers as input [54]. For each cell line, PCA was performed on the full dataset including all cells across all irradiation doses, in order to define a common reference space for all conditions. Specifically, the data were zero-centered (i.e., mean-centered) but not variance-standardized, so that features retain their original physical scaling. The resulting transformation was then used to project each cell into a shared low-dimensional space defined by the first two PCA components, from which dose-specific populations were subsequently extracted, as displayed in Fig. 4(a). As our goal was to define a dose-response curve, we performed pairwise comparisons of each irradiated cell population against the control population in the 2D PCA space, as shown in Fig. 4(b-f). Notably, the cluster of cells irradiated at a given X-ray dose shifts progressively further from the control cluster as the dose increases. However, to quantify this shift, it is necessary to account not only for the Euclidean distance between cluster centroids but also for the dispersion of each cluster. Accordingly, Fig. 4 also displays the covariance ellipse for each cluster, whose shape and orientation are determined by the eigenvectors and eigenvalues of the cluster covariance matrix. These ellipses provide a visual representation of the data's dispersion and correlation along the principal axes. For multivariate normal distributions, each ellipse corresponds to the 1-standard deviation contour around the cluster centroid. For example, the 0.25 Gy population in Fig. 4(b) exhibits the narrowest dispersion, while the 1 Gy population in Fig. 4(d) shows the largest one. In contrast, the 0.5 Gy, 1.5 Gy, and 2 Gy populations in Fig. 4(c,e,f), respectively, display a dispersion comparable to that of the control group. Therefore, to quantify differences among cell populations, we computed the FDR that takes into account not only the separation between cluster centroids but also the dispersion within each cluster, providing a robust measure of the overall distinction between populations.

In summary, as highlighted by the feature analysis in Fig. 3(b), individual biophysical markers exhibit non-monotonic and oscillatory behavior across irradiation doses, making them unsuitable as standalone dose–response indicators. This motivates the use of a multivariate approach that captures the collective variation of multiple features. At each irradiation dose D, the corresponding FDR_D quantifies the divergence of the irradiated cell population from the control population in the multidimensional space of HTFC biophysical features, reflecting how much the overall biophysical profile of irradiated cells differs from that of non-irradiated cells, rather than relying on any single feature (e.g., mean RI, volume, dry mass, or others). Accordingly, the curve formed by FDR_D values as a function of dose is defined here as the divergence score (DS) curve (Fig. 5(a)). From a methodological perspective, the DS is derived from the FDR, a multivariate measure widely used to quantify class separability in pattern recognition, as it accounts for both differences between population means and their intrinsic variability [47]. In biological applications, related concepts have been used to distinguish cellular states based on feature representations [55,56], while more recent image-based cell profiling studies rely on related notions of population distance in high-dimensional feature spaces [57]. However, their use as a continuous metric to construct a dose–response relationship is, to the best of our knowledge, not established. In this framework, we refer to the FDR as the DS to emphasize its interpretation as a dose-dependent measure of population deviation, enabling direct comparison with standard radiobiological dose–response profiles. By construction, increasing radiation dose leads to a progressive separation between irradiated and control populations in the HTFC feature space, resulting in higher DS values. This is confirmed in Fig. 5(a), where the DS curve shows the characteristic features of radiobiological dose–response relationships, including a monotonic increase with dose, a well-defined baseline at zero irradiation (DS = 0), and a nonlinear trend consistent with saturating or sigmoidal behavior. Taken together, these results indicate that the DS curve captures the magnitude of radiation-induced cellular perturbation while providing a label-free quantitative readout that reflects the fundamental properties of conventional dose–response assays. This supports its potential use as an alternative to standard clonogenic assays for evaluating radiation sensitivity. It is worth remarking that, in the present work, the uncertainty on the FDR (and thus on the DS) was estimated by propagating the variability of the sample means, while neglecting the contribution arising from the estimation of the covariance matrices. Neglecting covariance uncertainty represents a simplification of the full error propagation and may lead to a partial underestimation of the error bars, particularly in the case of moderate sample sizes and when covariance differs across doses. This choice was made to obtain a tractable analytical expression and relies on the assumption that, for sufficiently large sample sizes, the uncertainty associated with covariance estimation has a smaller impact than that of the mean vectors. In our case, the number of analysed cells per dose (Table S1) ranges from tens to over one hundred cells. Considering the low dimensionality of the PCA space ($d = 2$), together with the available sample size per condition, this supports a reasonably stable estimation of the covariance matrices, as the number of observations per dose is substantially larger than the number of parameters defining the covariance matrix, thereby limiting the impact of sampling variability. Importantly, this study is intended as a proof of concept. In this perspective, the number of analysed cells could be increased by several orders of magnitude by fully exploiting the high-throughput capability of flow cytometry at the basis of HTFC, which would further improve the robustness of both covariance estimation and uncertainty quantification. We also note that, in our experimental design, each dose corresponds to separate flasks, independently irradiated and measured in distinct HTFC experiments. Although all flasks originate from the same initial cell culture, the subsequent processing steps support the assumption that measurements across doses are largely independent, so that covariance estimation is not systematically biased by inter-dose correlations. Finally, we emphasize that the main conclusions of the study rely on the monotonic increase of the DS curve as a function of dose, rather than on the exact magnitude of the associated uncertainties. Therefore, while a more complete uncertainty propagation could affect the size of the error bars, it would not alter the observed dose-dependent trend nor the resulting interpretation.

3.3. Assessment of the divergence score as a label-free quantitative X-ray dose-response curve

The clonogenic assay is considered the gold standard in radiobiology (Franken, 2006). In this assay, single cells are seeded at low density and allowed to grow for 1–2 weeks, during which only cells that survive the

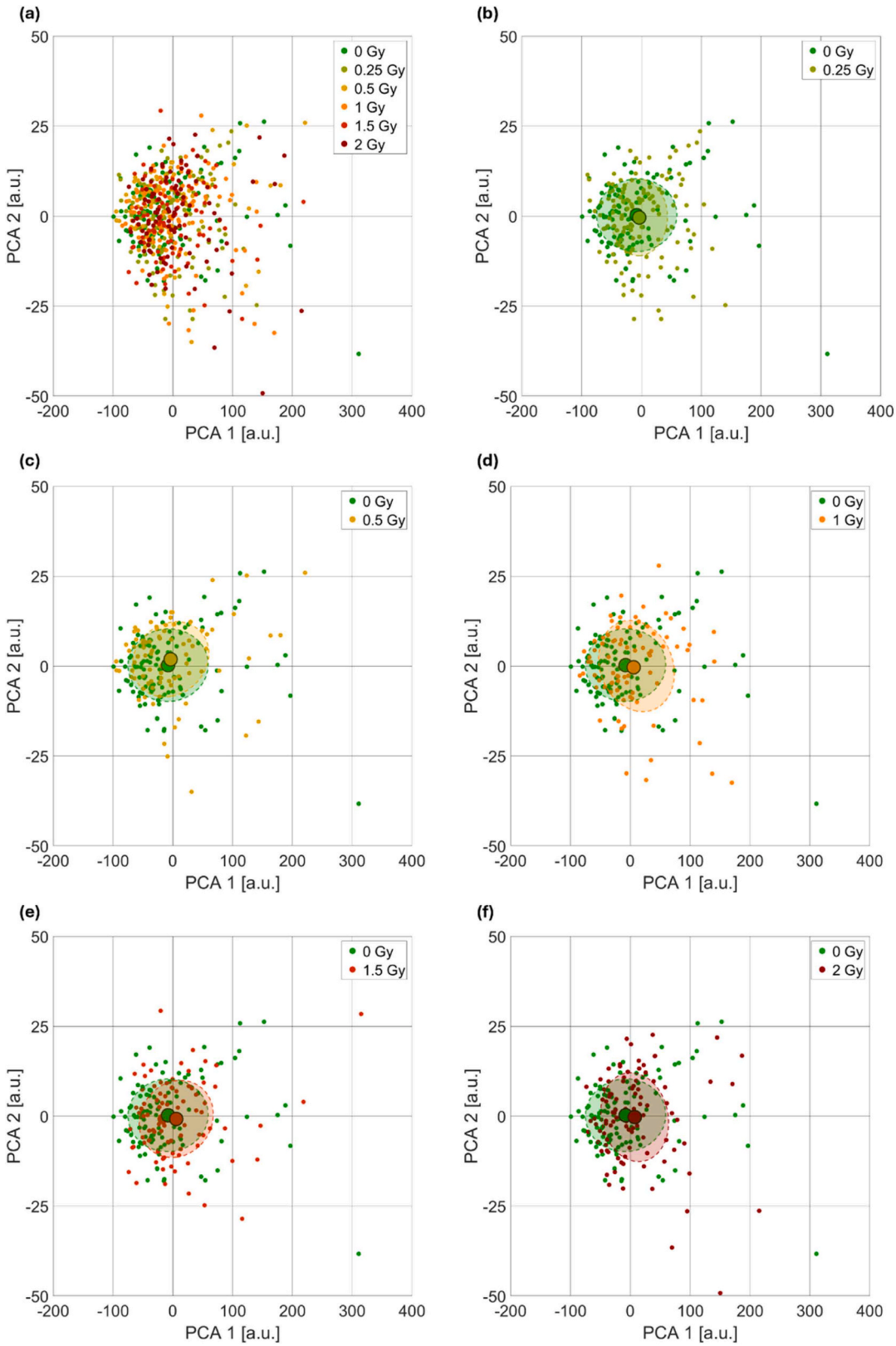

Fig. 4. Representation in the 2D PCA space of the neuroblastoma SKNBE2 cells exposed to different X-ray doses according to their HTFC-based biophysical characterization. (a) Comparison between the control population and the irradiated populations. (b) Comparison between the control population and the population irradiated at 0.25 Gy. (c) Comparison between the control population and the population irradiated at 0.5 Gy. (d) Comparison between the control population and the population irradiated at 1 Gy. (e) Comparison between the control population and the population irradiated at 1.5 Gy. (f) Comparison between the control population and the population irradiated at 2 Gy. For each cluster, the centroid and the covariance ellipse are highlighted. The number of analysed cells for each dose was as follows: 0 Gy (n = 109), 0.25 Gy (n = 127), 0.5 Gy (n = 83), 1 Gy (n = 87), 1.5 Gy (n = 87), and 2 Gy (n = 97). All HTFC data were obtained from a single independent experiment per dose.

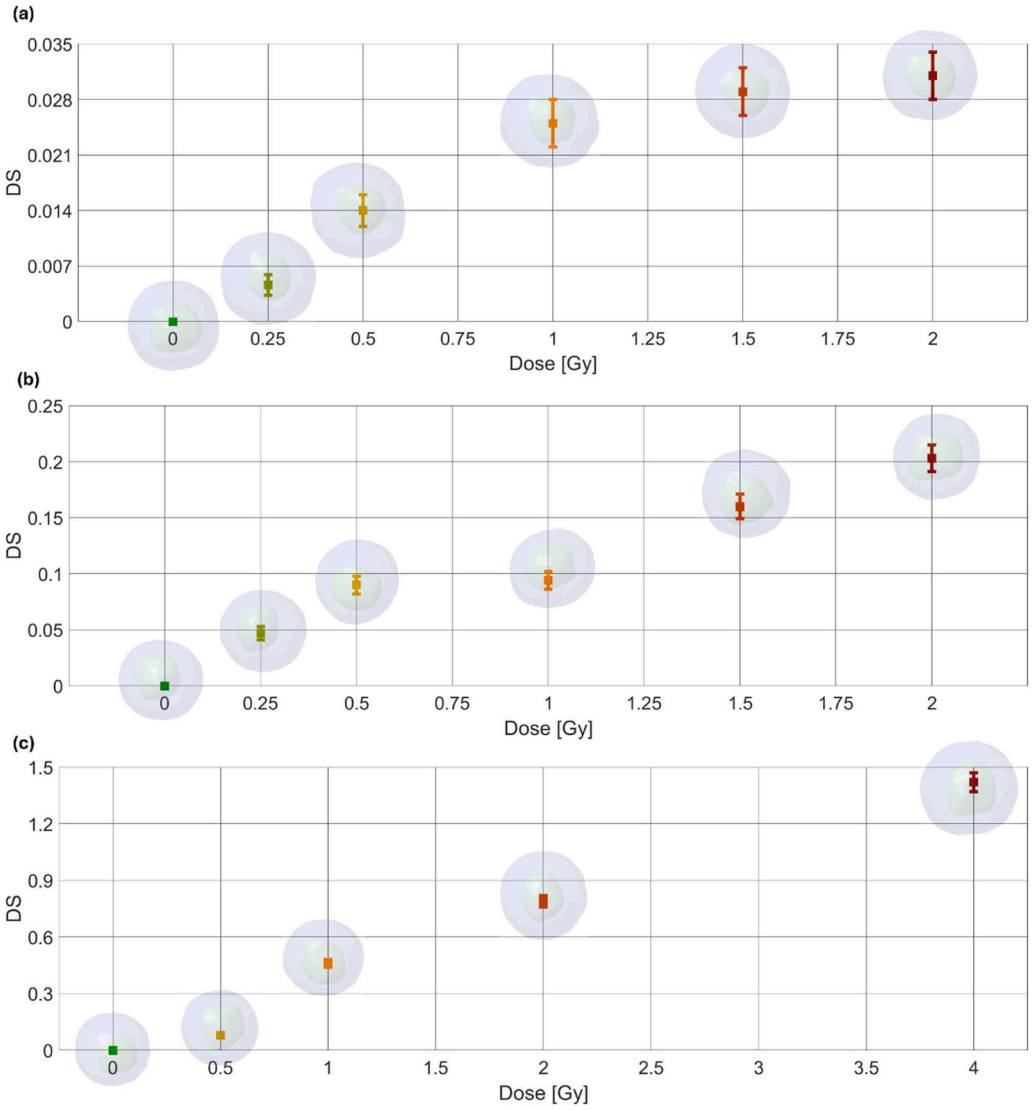

Fig. 5. Divergence Score (DS) curve computed by HTFC to serve as a label-free quantitative X-ray dose-response curve. (a) Neuroblastoma SKNBE2 cell line. (b) Breast cancer MCF7 cell line. (c) Neuroblastoma SHSY5Y cell line. The number of analysed SKNBE2 cells per dose was: 0 Gy (n = 109), 0.25 Gy (n = 127), 0.5 Gy (n = 83), 1 Gy (n = 87), 1.5 Gy (n = 87), and 2 Gy (n = 97); for MCF7 cells: 0 Gy (n = 44), 0.25 Gy (n = 89), 0.5 Gy (n = 116), 1 Gy (n = 115), 1.5 Gy (n = 75), and 2 Gy (n = 89); and for SHSY5Y cells: 0 Gy (n = 38), 0.5 Gy (n = 133), 1 Gy (n = 50), 2 Gy (n = 38), and 4 Gy (n = 24). All HTFC data were obtained from a single independent experiment per dose.

radiation insult and preserve their reproductive capacity give rise to colonies. Colonies are then fixed, stained, and manually counted. A parameter commonly employed in radiobiology to assess the response of a cell population to ionizing radiation is the surviving fraction (SF), which is conventionally measured through clonogenic assays. The SF is defined as the ratio between the number of colonies formed by irradiated cells and the number of seeded cells corrected for the plating efficiency. In other words, the SF quantifies the proportion of cells that retain the ability to undergo unlimited proliferation and form macroscopic colonies following radiation exposure. The resulting SF curve, obtained by plotting the SF values against the radiation dose, typically exhibits a decreasing trend confined within the [0,1] interval, reflecting the progressive loss of clonogenic potential with increasing radiation dose. The primary aim of the present work is not to establish a direct mapping between DS and SF, but rather to provide a proof-of-concept demonstration that a label-free biophysics-based metric (i.e., the DS) could capture consistent dose-dependent biological information that is in strong agreement with established radiobiological readouts (i.e., the SF). Hence, here we exploit the SF curve obtained by clonogenic assay (see Table S2) to assess the DS curve as a label-free quantitative X-ray dose-response curve. For the sole purpose of comparing the trend of the DS curve to the trend of the SF, we computed the normalized divergence score (NDS) as

$$\mathrm{NDS} = 1 - \frac{\mathrm{FDR}}{\mathrm{FDR}_{\max}}\,, \tag{9}$$

where $\mathrm{FDR}_{\max}$ is the maximum value of the DS curve in the observed dose range. As reported in Table S2, thanks to the normalization, the NDS value at 0 Gy is forced to be 1 and the NDS value at the highest irradiation dose is forced to be 0, thus reproducing a decreasing trend in the [0,1] interval.

Accordingly, the uncertainty on NDS_D, denoted as $\sigma_{\mathrm{NDS}_\mathrm{D}}$, was estimated using standard first-order error propagation. The total propagated uncertainty is given by

$$\sigma_{\mathrm{NDS}_\mathrm{D}} = \sqrt{\left(\frac{\partial \mathrm{NDS}_\mathrm{D}}{\partial \mathrm{FDR}_\mathrm{D}}\right)^2 \sigma^2_{\mathrm{FDR}_\mathrm{D}} + \left(\frac{\partial \mathrm{NDS}_\mathrm{D}}{\partial \mathrm{FDR}_{\max}}\right)^2 \sigma^2_{\mathrm{FDR}_{\max}}}\,, \tag{10}$$

which yields

$$\sigma_{NDS_D} = \sqrt{\left(\frac{1}{FDR_{max}}\right)^2 \sigma^2_{FDR_D} + \left(\frac{NDS_D}{FDR^2_{max}}\right)^2 \sigma^2_{FDR_{max}}}\,. \quad (11)$$

In Fig. 6(a,b), for the neuroblastoma SKNBE2 cell line, we report the SF and NDS curves, respectively. To evaluate the relationship between the two readouts, Fig. 6(c) shows their linear regression analysis by $y = m(x-1)+1$ equation, which yields a slope of 0.73 ± 0.03. This corresponds to a Pearson correlation coefficient 0.99 ± 0.01, confirming a very strong agreement between the trends of the two approaches despite intrinsic differences in their absolute values. We note that the Pearson correlation coefficient is invariant under linear transformations of the variables, thus the normalization introduced for the NDS does not affect the reported correlation values. In contrast, absolute error metrics such as MAE or RMSE are inherently dependent on the scale of the variables and on the chosen normalization. In fact, both the NDS and SF curve originate from a value of 1 at 0 Gy, reflecting the unperturbed state of the control population. However, while the SF curve progressively decreases with increasing dose and asymptotically approaches 0 (without necessarily reaching it in the dose range considered), the NDS curve is inherently normalized to span the [0,1] interval, with its minimum always equal to 0. The reason is that DS and SF arise from fundamentally different biological and methodological frameworks (namely, early biophysical alterations in viable cells versus long-term clonogenic reproductive capacity), therefore a direct error-based comparison would require a prior procedure to map one quantity onto the other, which is out of the scope of our research. In the absence of such mapping, absolute error metrics would not provide a fully meaningful or interpretable measure of agreement. Instead, the normalization was introduced solely for visualization purposes, to facilitate an intuitive comparison of the overall dose-dependent trends between two conceptually distinct readouts. It is not intended to imply quantitative equivalence or to enforce any direct relationship between DS and SF values.

To further validate our DS dose-response curve, we performed an additional experiment using a different cancer type by analysing breast cancer MCF7 cells. As summarized in Table S3, we collected 528 cells using the same irradiation doses as for the neuroblastoma SKNBE2 experiment. The DS curve for MCF7 cells (see Fig. 5(b)) exhibits the same characteristic features observed for the neuroblastoma SKNBE2 cell line (see Fig. 5(a)), showcasing the reproducibility of the proposed approach across different cell types. The corresponding SF and NDS curves for MCF7 cells are shown in Fig. S2(a,b), respectively (see also Table S4), yielding a slope of 0.65 ± 0.04, corresponding to a Pearson correlation coefficient 0.98 ± 0.03 (see Fig. S2(c)).

Finally, we extended the validation to a different neuroblastoma cell line (i.e., 283 SHSY5Y cells). To test the HTFC system under modified experimental conditions, we adjusted the irradiation interval, which was enlarged and down sampled. In particular, the intermediate doses of 0.25 Gy and 1.5 Gy were omitted, while the higher dose of 4 Gy was included, as summarized in Table S5. The resulting DS curve for the neuroblastoma SHSY5Y cells (see Fig. 5(c)) exhibits a nonlinear monotonic trend, similar to that observed for the neuroblastoma SKNBE2 cells in Fig. 5(a) and breast cancer MCF7 cells in Fig. 5(b), supporting the applicability of the DS curve as a label-free dose-response metric. To further corroborate this observation, we compared the corresponding SF and NDS curves for the neuroblastoma SHSY5Y cell line (see Fig. S3(a, b), respectively; see also Table S6). Regression analysis yielded a slope of 1.12 ± 0.16, corresponding to a Pearson correlation coefficient 0.94 ± 0.11 (see Fig. S3(c)), confirming a strong agreement between the traditional and label-free readouts despite the down sampled irradiation interval and the smaller single cells dataset. It is worth noting that the first two principal components capture most of the total variance in all datasets considered, namely 99.84% for SKNBE2, 99.78% for MCF7, and 99.25% for SHSY5Y cells. This indicates that the 2D PCA space provides an almost complete representation of the original high-dimensional feature space. To further assess the robustness of this choice, we progressively increased the number of retained components. For the SKNBE2 and MCF7 datasets, the monotonic dose–response behavior of the DS is already disrupted when the third principal component is included, whereas for SHSY5Y cells deviations from monotonicity emerge when higher-order components are considered (from approximately the ninth component onward). This behavior is consistent with the feature-level analysis in Fig. 3(b), which shows that individual biophysical markers exhibit non-monotonic and oscillatory trends across irradiation doses. Consequently, working in the full feature space (or equivalently including all PCA components) inevitably incorporates these oscillatory contributions, which can obscure the emergence of a clear dose–response relationship. In this framework, PCA acts as a dimensionality reduction step that isolates the dominant dose-related variability, while higher-order components primarily capture residual variability and noise. Therefore, restricting the analysis to the first two principal components, which account for more than 99% of the total variance, provides a robust and physically meaningful representation in which the DS exhibits a stable and monotonic behavior. In contrast, extending the analysis to the full feature space would reduce the interpretability of the DS as a dose–response metric and is not aligned with the goal of extracting a clear dose-dependent trend.

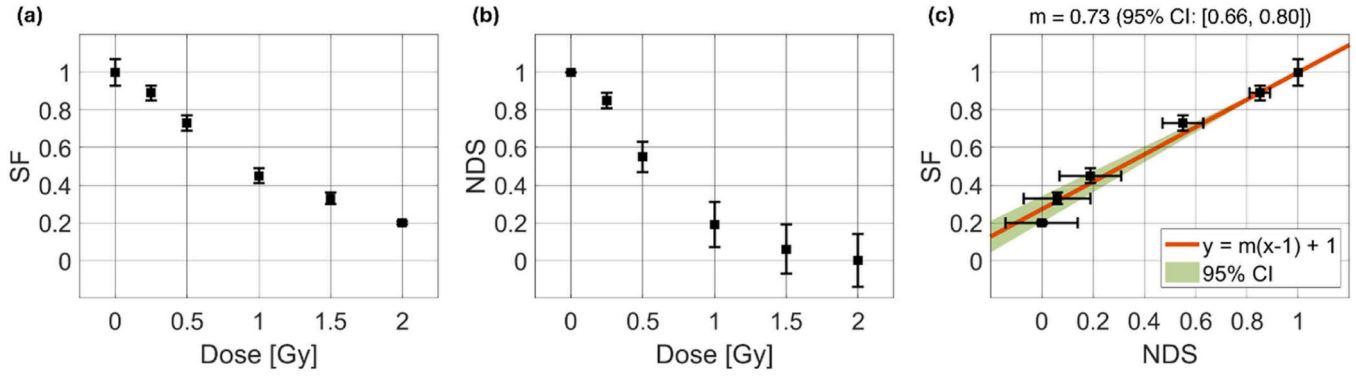

Fig. 6. Assessment of the label-free quantitative X-ray dose-response curve for the neuroblastoma SKNBE2 cell line. (a,b) Surviving Fraction (SF) and Normalized Divergence Score (NDS) curves, respectively. (c) Correlation between SF curve in (a) and NDS curve in (b). For the NDS curves, the number of analysed SKNBE2 cells per dose was: 0 Gy (n = 109), 0.25 Gy (n = 127), 0.5 Gy (n = 83), 1 Gy (n = 87), 1.5 Gy (n = 87), and 2 Gy (n = 97); for MCF7 cells: 0 Gy (n = 44), 0.25 Gy (n = 89), 0.5 Gy (n = 116), 1 Gy (n = 115), 1.5 Gy (n = 75), and 2 Gy (n = 89); and for SHSY5Y cells: 0 Gy (n = 38), 0.5 Gy (n = 133), 1 Gy (n = 50), 2 Gy (n = 38), and 4 Gy (n = 24). All HTFC data for the NDS curves were obtained from a single independent experiment per dose. For the SF curves, three flasks were seeded at identical cell density and irradiated at each dose to provide independent replicates.

4. Conclusions

We introduced a novel approach to quantify radiation-induced cellular alterations by establishing a label-free quantitative X-ray dose-response curve from HTFC 3D quantitative single-cell analysis. By exploiting 3D RI tomograms, we extracted a panel of biophysical markers descriptive of both whole-cell and intracellular compartments. Through PCA and FDR, we defined a DS metric that captures the deviation of irradiated cell populations from non-irradiated controls in a multidimensional biomarker space, thus showing a duality behavior with respect to the gold-standard dose-response profile. In fact, the DS curve consistently displayed the hallmark properties of radiobiological dose–response relationships, i.e. monotonicity, nonlinearity, and a defined baseline at zero dose. Importantly, when normalized for assessment purposes, the DS curve showed strong correlations with gold-standard clonogenic survival curves across three model cancer cell lines (neuroblastoma SHSY5Y cells, neuroblastoma SKNBE2 cells, and breast cancer MCF7 cells), with Pearson correlation coefficients ranging from 0.94 to 0.99. These results confirm that HTFC-derived DS curves can serve as reliable label-free alternative to standard clonogenic assays.

Compared to conventional assays, the HTFC approach provides several critical advantages. First, its label-free aspect eliminates the need for exogenous dyes, thus avoiding issues such as photobleaching, phototoxicity, or interference with downstream analyses. Second, it is rapid as it enables acquisition and analysis of hundreds/thousands of single cells within 24 h after irradiation, whereas clonogenic assays typically require 1–2 weeks. Third, it is operator-independent, providing an objective, automated readout that reduces bias inherent in colony counting. Moreover, clonogenic assays provide an indirect measure of radiosensitivity by quantifying the fraction of cells that retain the ability to proliferate after irradiation, thus reflecting only the ultimate cell death outcome. In contrast, HTFC allows to directly evaluate the radiation-induced alterations in viable cells before they reach the death state, offering in principle a dynamic view of those biophysical and morphological changes that typically precede the loss of clonogenic potential. By extracting a rich set of intracellular biophysical markers, HTFC goes beyond survival metrics, offering detailed insights into 3D morphological and RI changes associated with radiation damage at subcellular level.

Unlike conventional biosensors that rely on indirect readouts based on molecular probes or fluorescent labels, HTFC combines physical optics with flow cytometry to directly measure cell states in a minimally invasive manner. In this study, we observed a strong correlation between the DS curve and the standard SF curve (>90%). In classical radiobiology, however, cell survival following irradiation is typically modeled by fitting SF data with the linear–quadratic (LQ) model [40] or other advanced approaches [58]. For example, the LQ formalism expresses the logarithm of the SF as the sum of a linear term (αD), representing irreparable lethal damage proportional to dose, and a quadratic term (βD^2), which accounts for sublethal damage that becomes lethal when accumulated or misrepaired. The α/β ratio is widely regarded as a key indicator of radiosensitivity to guide clinical dose-fractionation strategies, distinguishing tissues or tumors with predominantly linear (early responding) vs. quadratic (late responding) damage responses [59]. Parameters of the LQ model are shown as example in Fig. S1(a-c), corresponding to the SF curves of the three model cell lines analyzed in this study. However, the same radiobiological models cannot be directly applied to the DS dose-response curve, since its biological meaning differs from that of the SF curve. Clonogenic assays quantify the long-term reproductive survival of irradiated cells, measuring the fraction of cells that retain the ability to proliferate after radiation exposure. In contrast, HTFC provides an early assessment, as it quantifies radiation-induced alterations in the biophysical properties of cells that remain viable 24 h after treatment. Thus, while SF reflects the ultimate proliferative capacity of a population, DS captures short-term phenotypic and structural changes in surviving cells. Importantly, in this study we do not aim to establish a direct quantitative mapping between DS and SF, but rather to demonstrate that DS captures consistent dose-dependent biological information that follows trends comparable to established radiobiological readouts. Therefore, future work will focus on identifying and calibrating the most suitable model curves to translate DS-derived biological responses into precise dose-response parameters across different cell lines and tissue types. This will require a dedicated modeling framework and larger datasets enabling predictive validation (e.g., across independent experiments or acquisition days). Additionally, ongoing studies will aim to extend and validate this label-free approach using cells derived from patient biopsies. In conclusion, we have demonstrated that HTFC-derived DS curves offer a label-free, rapid, and operator-independent assay that could in future improve the classical and well-assessed clonogenic survival analyses. This study provides a proof-of-concept demonstration of the potential of DS as a label-free descriptor of radiation response, laying the groundwork for future predictive applications. These preliminary results suggest that, with further validation and calibration, HTFC could evolve into a next-generation biosensor capable of rapidly profiling tumor radiosensitivity from patient-derived samples and supporting the development of precision oncology strategies in personalized RT. In future, HTFC technology could in part replace fluorescence based IFC as it provides informative content in all the applications that concern morphological and density variation in cell populations. HTFC would be particularly suitable in characterizing cell phenotypes induced by gene modification, drug treatments or by exposure to pollutants. In cell biology HTFC would be pivotal in identify the onset of subcellular compartment as lipids droplets or vacuoles, or to detect the uptake of external particles by deciphering their 3D network.

CRediT authorship contribution statement

Pietro Ferraro: Writing – review & editing, Writing – original draft, Supervision, Project administration, Funding acquisition, Conceptualization. **Giusy Giugliano:** Writing – review & editing, Writing – original draft, Methodology, Investigation. **Rocco Mottareale:** Investigation. **Chiara de Vita:** Writing – original draft, Resources, Investigation. **Daniele Pirone:** Writing – review & editing, Writing – original draft, Visualization, Software, Investigation, Formal analysis, Conceptualization. **Pasquale Memmolo:** Writing – review & editing, Supervision, Software, Methodology. **Vittorio Bianco:** Writing – review & editing, Software. **Simonetta Grilli:** Writing – review & editing. **Gennaro Giordano:** Investigation. **Lisa Miccio:** Writing – review & editing, Supervision, Methodology, Conceptualization. **Mariagabriella Pugliese:** Writing – review & editing, Writing – original draft, Supervision, Methodology, Conceptualization. **Marco Durante:** Writing – review & editing, Writing – original draft, Supervision, Project administration, Funding acquisition, Conceptualization.

Declaration of Competing Interest

The authors declare that they have no known competing financial interests or personal relationships that could have appeared to influence the work reported in this paper.

Acknowledgments

This work was supported by project PRIN 2022 PNRR - Flow-cytometry ImaGing by Holographic tomography for predicting TUMor control in Oncology patients treated with Radiotheraphy (FIGHT-TUMOR), Prot. P2022ATE2J – funded by the Italian Ministry of University & Research in the framework of Next Generation EU.

Additional information

Supplementary data to this article can be found in the Supplementary

Information.

Appendix A. Supporting information

Supplementary data associated with this article can be found in the online version at doi:10.1016/j.snb.2026.140232.

Data availability

Data will be made available on request.

References

[1] S.J. Altschuler, L.F. Wu, Cellular heterogeneity: do differences make a difference? Cell 141 (4) (2010) 559–563, https://doi.org/10.1016/j.cell.2010.04.033.

[2] D. Wang, S. Bodovitz, Single cell analysis: the new frontier in 'omics', Trends Biotechnol. 28 (6) (2010) 281–290, https://doi.org/10.1016/j.tibtech.2010.03.002.

[3] M.G. Macey, Principles of flow cytometry. Flow Cytometry: Principles and Applications, Humana Press, Totowa, NJ, 2007, pp. 1–15, https://doi.org/10.1007/978-1-59745-451-3_1.

[4] P. Rees, H.D. Summers, A. Filby, A.E. Carpenter, M. Doan, Imaging flow cytometry, Nat. Rev. Methods Prim. 2 (1) (2022) 86, https://doi.org/10.1038/s43586-022-00167-x.

[5] M. Doan, I. Vorobjev, P. Rees, A. Filby, O. Wolkenhauer, A.E. Goldfeld, H. Hennig, Diagnostic potential of imaging flow cytometry, Trends Biotechnol. 36 (7) (2018) 649–652, https://doi.org/10.1016/j.tibtech.2017.12.008.

[6] Q. Wang, M.A. Rodrigues, M. Repin, S. Pampou, L.A. Beaton-Green, J. Perrier, R. C. Wilkins, Automated triage radiation biodosimetry: integrating imaging flow cytometry with high-throughput robotics to perform the cytokinesis-block micronucleus assay, Radiat. Res. 191 (4) (2019) 342–351, https://doi.org/10.1667/RR15243.1.

[7] R.C. Wilkins, M.A. Rodrigues, L.A. Beaton-Green, The application of imaging flow cytometry to high-throughput biodosimetry, Genome Integr. 8 (2017) 7, https://doi.org/10.4103/2041-9414.198912.

[8] R.C. Wilkins, L.A. Beaton-Green, Development of high-throughput systems for biodosimetry, Radiat. Prot. Dosim. 199 (14) (2023) 1477–1484, https://doi.org/10.1093/rpd/ncad060.

[9] H.M. Swartz, B.B. Williams, A.B. Flood, Overview of the principles and practice of biodosimetry, Radiat. Environ. Biophys. 53 (2) (2014) 221–232, https://doi.org/10.1007/s00411-014-0522-0.

[10] M. Durdik, P. Kosik, L. Jakl, M. Kozackova, E. Markova, K. Vigasova, I. Belyaev, Imaging flow cytometry and fluorescence microscopy in assessing radiation response in lymphocytes from umbilical cord blood and cancer patients, Cytom. Part A 99 (12) (2021) 1198–1208, https://doi.org/10.1002/cyto.a.24468.

[11] Y. Lee, Q. Wang, I. Shuryak, D.J. Brenner, H.C. Turner, Development of a high-throughput γ-H2AX assay based on imaging flow cytometry, Radiat. Oncol. 14 (1) (2019) 150, https://doi.org/10.1186/s13014-019-1344-7.

[12] A. Gilbert, V. Payet, B. Bernay, E. Chartier-Garcia, I. Testard, S.M. Candéias, F. Chevalier, Label-free direct mass spectrometry analysis of the bystander effects induced in chondrocytes by chondrosarcoma cells irradiated with X-rays and carbon ions, Front. Biosci. -Landmark 27 (9) (2022) 277, https://doi.org/10.31083/j.fbl2709277.

[13] I. Delfino, G. Perna, V. Ricciardi, M. Lasalvia, L. Manti, V. Capozzi, M. Lepore, X-ray irradiation effects on nuclear and membrane regions of single SH-SY5Y human neuroblastoma cells investigated by Raman micro-spectroscopy, J. Pharm. Biomed. Anal. 164 (2019) 557–573, https://doi.org/10.1016/j.jpba.2018.11.028.

[14] G. Macke, M. Sheth, M. Sharma, S. Kongsomros, M. Lehn, T.M. Wise-Draper, L. Esfandiari, Label-free monitoring of therapy response in 3D spheroids using lab-on-a-chip impedance spectroscopy, bioRxiv 2025 (09) (2025), https://doi.org/10.1101/2025.09.08.674936.

[15] N.T. Shaked, S.A. Boppart, L.V. Wang, J. Popp, Label-free biomedical optical imaging, Nat. Photonics 17 (12) (2023) 1031–1041, https://doi.org/10.1038/s41566-023-01299-6.

[16] Y. Park, C. Depeursinge, G. Popescu, Quantitative phase imaging in biomedicine, Nat. Photonics 12 (10) (2018) 578–589, https://doi.org/10.1038/s41566-018-0253-x.

[17] E. Ahamadzadeh, K. Jaferzadeh, S. Park, S. Son, I. Moon, Automated analysis of human cardiomyocytes dynamics with holographic image-based tracking for cardiotoxicity screening, Biosens. Bioelectron. 195 (2022) 113570, https://doi.org/10.1016/j.bios.2021.113570.

[18] M.K. Kim, Principles and techniques of digital holographic microscopy, SPIE Rev. 1 (1) (2010) 018005, https://doi.org/10.1117/6.0000006.

[19] G. Kim, Y. Jo, H. Cho, H.S. Min, Y. Park, Learning-based screening of hematologic disorders using quantitative phase imaging of individual red blood cells, Biosens. Bioelectron. 123 (2019) 69–76, https://doi.org/10.1016/j.bios.2018.09.068.

[20] B. Gul, S. Ashraf, S. Khan, H. Nisar, I. Ahmad, Cell refractive index: models, insights, applications and future perspectives, Photo Photodyn. Ther. 33 (2021) 102096, https://doi.org/10.1016/j.pdpdt.2020.102096.

[21] P.Y. Liu, L.K. Chin, W. Ser, H.F. Chen, C.M. Hsieh, C.H. Lee, Y. Leprince-Wang, Cell refractive index for cell biology and disease diagnosis: past, present and future, Lab a Chip 16 (4) (2016) 634–644, https://doi.org/10.1039/C5LC01445J.

[22] T. Kawase, K. Okuda, M. Nagata, M. Tsuchimochi, H. Yoshie, K. Nakata, Non-invasive, quantitative assessment of the morphology of γ-irradiated human mesenchymal stem cells and periosteal cells using digital holographic microscopy, Int. J. Radiat. Biol. 92 (12) (2016) 796–805, https://doi.org/10.1080/09553002.2016.1230242.

[23] Z. Hormozi-Moghaddam, S.M. Taheri, A. Neshasteh-Riz, V.F. Rad, M. Shaghaghi, Assessment of morphological changes in breast cancer cells following X-ray radiation utilizing digital holographic microscopy, Front. Biomed. Technol. (2024), https://doi.org/10.18502/fbt.v12i1.17740.

[24] X. Xiao, L. Che, Y. Li, R. Peng, M. Wang, W. Xiao, H. Wang, Label-free observation of morphological alteration of irradiated-urothelial bladder carcinoma cells through digital holographic microscopy, Front. Phys. 10 (2022) 925523, https://doi.org/10.3389/fphy.2022.925523.

[25] D. Pirone, G. La Verde, J. Behal, C. Arrichiello, P. Muto, I. Kurelac, M. Pugliese, Estimating the effects of x-ray radiations on lymphocytes by minimally invasive holographic imaging flow cytometry, J. Phys. D Appl. Phys. 57 (50) (2024) 505402, https://doi.org/10.1088/1361-6463/ad7c56.

[26] G. Kim, H. Hugonnet, K. Kim, J.H. Lee, S.S. Lee, J. Ha, Y. Park, Holotomography, Nat. Rev. Methods Prim. 4 (1) (2024) 51, https://doi.org/10.1038/s43586-024-00327-1.

[27] D. Jin, R. Zhou, Z. Yaqoob, P.T. So, Tomographic phase microscopy: principles and applications in bioimaging, J. Opt. Soc. Am. B 34 (5) (2017) B64–B77, https://doi.org/10.1364/JOSAB.34.000B64.

[28] V. Balasubramani, A. Kuś, H.Y. Tu, C.J. Cheng, M. Baczewska, W. Krauze, M. Kujawińska, Holographic tomography: techniques and biomedical applications, Appl. Opt. 60 (10) (2021) B65–B80, https://doi.org/10.1364/AO.416902.

[29] F. Borrelli, G. Giugliano, E. Houliez, J. Behal, D. Pirone, L. Roselli, P. Ferraro, 3D holographic flow cytometry measurements of microalgae: strategies for angle recovery in complex rotation patterns, Lab a Chip 25 (2025) 5283–5291, https://doi.org/10.1039/D5LC00559K.

[30] P. Memmolo, D. Pirone, D.G. Sirico, L. Miccio, V. Bianco, A.B. Ayoub, P. Ferraro, Loss minimized data reduction in single-cell tomographic phase microscopy using 3D Zernike descriptors, Intell. Comput. 2 (2023) 0010, https://doi.org/10.34133/icomputing.0010.

[31] D. Pirone, J. Lim, F. Merola, L. Miccio, M. Mugnano, V. Bianco, P. Ferraro, Stain-free identification of cell nuclei using tomographic phase microscopy in flow cytometry, Nat. Photonics 16 (12) (2022) 851–859, https://doi.org/10.1038/s41566-022-01096-7.

[32] D. Pirone, M.M. Villone, P. Memmolo, Z. Wang, V. Tkachenko, W. Xiao, P. L. Maffettone, On the hydrodynamic mutual interactions among cells for high-throughput microfluidic holographic cyto-tomography, Opt. Lasers Eng. 158 (2022) 107190, https://doi.org/10.1016/j.optlaseng.2022.107190.

[33] D. Pirone, L. Xin, V. Bianco, L. Miccio, W. Xiao, L. Che, P. Ferraro, Identification of drug-resistant cancer cells in flow cytometry combining 3D holographic tomography with machine learning, Sens. Actuators B Chem. 375 (2023) 132963, https://doi.org/10.1016/j.snb.2022.132963.

[34] D. Pirone, C. Di Natale, M. Di Summa, N. Mosca, G. Giugliano, M. Schiavo, P. Ferraro, From genotype to phenotype: decoding mutations in blasts by holo-tomographic flow cytometry, Light Sci. Appl. 14 (1) (2025) 233, https://doi.org/10.1038/s41377-025-01913-y.

[35] D. Pirone, M. Schiavo, G. Giugliano, S. Montefusco, L. Miccio, P. Memmolo, P. Ferraro, Drug-induced reversible lysosomal changes tracked in live cells by holo-tomographic flow cytometry, ACS Nano (2025), https://doi.org/10.1021/acsnano.5c08530.

[36] V.R. Samuel, K.J. Rao, A review on label free biosensors, Biosens. Bioelectron. X 11 (2022) 100216, https://doi.org/10.1016/j.biosx.2022.100216.

[37] M. Baumann, M. Krause, J. Overgaard, J. Debus, S.M. Bentzen, J. Daartz, T. Bortfeld, Radiation oncology in the era of precision medicine, Nat. Rev. Cancer 16 (4) (2016) 234–249, https://doi.org/10.1038/nrc.2016.18.

[38] M. Durante, R. Orecchia, J.S. Loeffler, Charged-particle therapy in cancer: clinical uses and future perspectives, Nat. Rev. Clin. Oncol. 14 (8) (2017) 483–495, https://doi.org/10.1038/nrclinonc.2017.30.

[39] N.A. Franken, H.M. Rodermond, J. Stap, J. Haveman, C. Van Bree, Clonogenic assay of cells in vitro, Nat. Protoc. 1 (5) (2006) 2315–2319, https://doi.org/10.1038/nprot.2006.339.

[40] S.J. McMahon, The linear quadratic model: usage, interpretation and challenges, Phys. Med. & Biol. 64 (1) (2018) 01TR01, https://doi.org/10.1088/1361-6560/aaf26a.

[41] P. Memmolo, C. Distante, M. Paturzo, A. Finizio, P. Ferraro, B. Javidi, Automatic focusing in digital holography and its application to stretched holograms, Opt. Lett. 36 (10) (2011) 1945–1947, https://doi.org/10.1364/OL.36.001945.

[42] W. Zhou, Y. Yu, A. Asundi, Study on aberration suppressing methods in digital micro-holography, Opt. Lasers Eng. 47 (2) (2009) 264–270, https://doi.org/10.1016/j.optlaseng.2008.04.026.

[43] Q. Kemao, Windowed Fourier transform for fringe pattern analysis, Appl. Opt. 43 (13) (2004) 2695–2702, https://doi.org/10.1364/AO.43.002695.

[44] J.M. Bioucas-Dias, G. Valadao, Phase unwrapping via graph cuts, IEEE Trans. Image Process 16 (3) (2007) 698–709, https://doi.org/10.1109/TIP.2006.888351.

[45] D. Pirone, L. Miccio, V. Bianco, P. Ferraro, P. Memmolo, Self-consistent automatic retrieval of single-cell rotation enables highly reliable holo-tomographic flow cytometry, Opt. Lett. 50 (21) (2025) 6682–6685, https://doi.org/10.1364/OL.568696.

[46] R. Schofield, L. King, U. Tayal, I. Castellano, J. Stirrup, F. Pontana, E. Nicol, Image reconstruction: Part 1–understanding filtered back projection, noise and image acquisition, J. Cardiovasc. Comput. Tomogr. 14 (3) (2020) 219–225, https://doi.org/10.1016/j.jcct.2019.04.008.

[47] S. Theodoridis, Classification: a tour of the classics, in: S. Theodoridis (Ed.), Machine Learning: A Bayesian and Optimization Perspective, Academic Press, London, 2015, pp. 275–325, https://doi.org/10.1016/B978-0-12-818803-3.00016-7.
[48] U. Ritgen, Gaussian error propagation. Analytical Chemistry II, Springer, Berlin, Heidelberg, 2025, https://doi.org/10.1007/978-3-662-68710-9_19.
[49] D. Kim, S. Lee, M. Lee, J. Oh, S.A. Yang, Y. Park, Holotomography: refractive index as an intrinsic imaging contrast for 3-D label-free live cell imaging. Advanced Imaging and Bio Techniques for Convergence Science, Springer Singapore, Singapore, 2021, pp. 211–238, https://doi.org/10.1007/978-981-33-6064-8_10.
[50] D. Pirone, V. Bianco, L. Miccio, P. Memmolo, D. Psaltis, P. Ferraro, Beyond fluorescence: advances in computational label-free full specificity in 3D quantitative phase microscopy, Curr. Opin. Biotechnol. 85 (2024) 103054, https://doi.org/10.1016/j.copbio.2023.103054.
[51] B. Bai, X. Yang, Y. Li, Y. Zhang, N. Pillar, A. Ozcan, Deep learning-enabled virtual histological staining of biological samples, Light Sci. Appl. 12 (1) (2023) 57, https://doi.org/10.1038/s41377-023-01104-7.
[52] S. Adjemian, T. Oltean, S. Martens, B. Wiernicki, V. Goossens, T. Vanden Berghe, P. Vandenabeele, Ionizing radiation results in a mixture of cellular outcomes including mitotic catastrophe, senescence, methuosis, and iron-dependent cell death, Cell Death & Dis. 11 (11) (2020) 1003, https://doi.org/10.1038/s41419-020-03209-y.
[53] M. Robnik-Šikonja, I. Kononenko, Theoretical and empirical analysis of ReliefF and RReliefF, Mach. Learn. 53 (1) (2003) 23–69, https://doi.org/10.1023/A:1025667309714.
[54] M. Greenacre, P.J. Groenen, T. Hastie, A.I. d'Enza, A. Markos, E. Tuzhilina, Principal component analysis, Nat. Rev. Methods Prim. 2 (1) (2022) 100, https://doi.org/10.1038/s43586-022-00184-w.
[55] C. Conrad, H. Erfle, P. Warnat, N. Daigle, T. Lörch, J. Ellenberg, R. Eils, Automatic identification of subcellular phenotypes on human cell arrays, Genome Res. 14 (6) (2004) 1130–1136.
[56] M.V. Boland, R.F. Murphy, A neural network classifier capable of recognizing the patterns of all major subcellular structures in fluorescence microscope images of HeLa cells, Bioinformatics 17 (12) (2001) 1213–1223.
[57] J.C. Caicedo, S. Cooper, F. Heigwer, S. Warchal, P. Qiu, C. Molnar, A.E. Carpenter, Data-analysis strategies for image-based cell profiling, Nat. Methods 14 (9) (2017) 849–863.
[58] B. Andisheh, M. Edgren, D. Belkić, P. Mavroidis, A. Brahme, B.K. Lind, A comparative analysis of radiobiological models for cell surviving fractions at high doses, Technol. Cancer Res. & Treat. 12 (2) (2013) 183–192, https://doi.org/10.7785/tcrt.2012.500306.
[59] R.B. Hawkins, Effect of heterogeneous radio sensitivity on the survival, alpha beta ratio and biologic effective dose calculation of irradiated mammalian cell populations, Clin. Transl. Radiat. Oncol. 4 (2017) 32–38, https://doi.org/10.1016/j.ctro.2017.03.001.

Daniele Pirone received the M.S. degree in Biomedical Engineering in Italy from the University of Naples "Federico II" in 2019. In 2023, he earned the Ph.D. degree in "Information and Communication Technology for Health" from the same university. His doctoral thesis was recognized as the Best Ph.D. Thesis 2023 by the IEEE Photonics Italy Chapter. Since 2020, he has been affiliated with the Institute of Applied Sciences and Intelligent Systems (ISASI) of the Italian National Research Council (CNR), first as a Research Fellow, then as a Postdoctoral Researcher, and currently as a fixed-term Researcher. His research interests span image processing, computer vision, and artificial intelligence, with a particular focus on label-free computational microscopy, digital holography, quantitative phase imaging, phase contrast tomography, imaging flow cytometry, and Fourier ptychographic microscopy for biomedical and environmental applications. He has coauthored more than 100 publications in these areas.

Chiara de Vita earned her master's degree in physics, majoring in biomedical physics, from the University of Naples Federico II where she received a post-graduate research fellowship. Her main research interest is radiobiology.

Rocco Mottareale: is a physicist specializing in Medical Physics, working in the field of radiotherapy. His professional activities include clinical work, treatment plan optimization, and the dosimetry of ionizing radiation. He is involved in both clinical and translational research, leveraging radiomics and dosiomics approaches to enhance clinical decision-making, improve treatment personalization, and deepen the understanding of biological responses to radiation. His interests also extend to fundamental research, with a particular focus on radiobiology and the interactions between ionizing radiation and cellular structures

Giusy Giugliano received the B.S. degree in Information, Biomedical and Telecommunications Engineering from University of Naples "Parthenope", Naples, Italy, in 2019, and the M.S. degree in biomedical engineering from University of Naples "Federico II", Naples, in 2022. She is currently working toward the Ph.D. degree in Mathematics, Physics and Engineering Applications with the University of Campania "Luigi Vanvitelli", Caserta, Italy. In 2022, she has official collaboration with Institute of Applied Science and Intelligent Systems (ISASI) of the Italian National Research Council (CNR). Her research interests include developing advanced optical imaging and AI-driven methodologies for microscopic visualization and analysis, encompassing the design of computational microscopes and holographic techniques.

Gennaro Giordano earned his master's degree in Medical Biotechnology from the University of Naples Federico II. He is currently pursuing a PhD in Biochemistry and Biotechnology at the University of Campania "Luigi Vanvitelli". His main research interests are molecular and cellular biology.

Simonetta Grilli received the degree in physics from the University of Naples "Federico II", Italy, and the Ph.D. degree from the KTH in Stockholm, Sweden. She is currently director of research at the Institute of Applied Sciences and Intelligent Systems of CNR, Pozzuoli, Italy. The main research topics include biosensors, electro-hydrodynamics, inkjet printing, ferroelectric crystals, optical microscopy. Her current activities include innovative microfluidic platforms driven by pyroelectric fields. She is co-author of more than 250 publications on peer-reviewed journals.

Vittorio Bianco received the M.S. degree (cum laude) in Telecommunications Engineering from the University "Federico II" of Naples, Naples, Italy, and the Ph.D. degree in Materials and Structures Engineering in 2016. He won the IEEE Best Doctoral Thesis in Optoelectronics 2016 Award. In 2023 he was awarded as best italian young researcher in the field "AI, Big Data and High Performance Computing". He has performed research in different labs in Italy, Germany and USA, gaining team-work skills, independence and responsibility attitudes in carrying out project activities. In 2011, he worked with the German Aerospace Center, Munich, Germany, in the fields of SAR interferometry and tomography. In 2017, he was a Postdoc with the University of California, Los Angeles (UCLA), USA, working in the field of lensless inline holographic flow cytometry for point of care diagnostics and water quality monitoring. Since 2012, he has been with the Italian National Research Council, where he is currently working at ISASI. VB's research interests include the fields of quantitative phase imaging (QPI), optical systems engineering, image processing and computational microscopy, digital holography, Fourier Ptychographic Microscopy, in-flow holographic tomography, bio-speckle analysis, AI applied to microfluidics, Lab on a Chip imaging, single-cell analysis, medical diagnostics and environmental monitoring. He coauthored more than 300 works in his field of expertise.

Lisa Miccio is Physicist working in Applied Optic field. Her main research interests are in the area of Quantitative Phase Microscopy and Tomography. Scientific activities concern the investigation of label-free approaches for imaging in biomedical application, industrial inspection and cultural heritage. In 2006 she obtained Physics degree from the University of Naples "Federico II" (Italy) and in 2010 an International PhD from the University of Florence (Italy). She has been visiting scholar at Universidad Complutense in Madrid (Spain) during the PhD school and at University of Munster (Germany) in the framework of Horizon 2020 cost action. Currently, she is Senior Researcher at Italian National Research Council – Institute of Applied Sciences and Intelligent Systems (CNR-ISASI). She is co-author of more than 100 peer-review papers; she attended more than 60 international conferences, she is supervisor of PhD students and research fellows. She is member of the SPIE and OPTICA Societies and serves these societies as member of technical and program committees and as Chair.

Pasquale Memmolo received the Ph.D. degree in electronic and telecommunication engineering from the University of Naples "Federico II", Naples, Italy, in 2012. He is currently the Research Director with the Institute of Applied Sciences and Intelligent Systems "Eduardo Caianiello" (ISASI-CNR,), Pozzuoli, Italy. He has coauthored more than 100 articles in peer-reviewed journals and more than 200 conference papers. His research interests include computational microscopy, ranging across different topics including digital holography, holographic tomography, Fourier ptychographic microscopy, microfluidics, optical engineering, advanced image processing, and artificial intelligence

Mariagabriella Pugliese is an associate professor of Applied Physics at the University of Naples Federico II. Her research focuses on radiobiology and radiation protection. MP is a former President of the Italian Society for Radiation Research and is the author of over 200 publications in scientific journals.

Marco Durante is Director of the Biophysics Department at GSI Helmholtz Center for Heavy Ion Research (Darmstadt, Germany), Full Professor of Physics at the Technical University of Darmstadt and at the University of Naples Federico II in Italy, and Adjunct Professor at the Gunma College of Medicine in Japan. He is generally recognized as world leader in the field of particle radiobiology and medical physics. He is co-author of over 500 papers in peer-reviewed scientific journals and received many awards for his research efforts. He was President of the International Association for Radiation research (IARR) 2011–2015 and is currently President of the Particle Therapy Co-Operative Group (PTCOG).

Pietro Ferraro (Senior Member, IEEE) received the degree (cum laude) in physics from the University of Naples Federico II, Naples, Italy, in 1987. He founded the Institute of Applied Sciences and Intelligent Systems of CNR, Pozzuoli, Italy. From 2014–2019, he was the Director. He is currently a Research Director of ISASI, Pozzuoli, Italy. He has authored or coauthored more than 320 articles in peer-reviewed journals and more than 200 conference papers. His research interests include digital holography, microscopy, laser interferometry, lithography, ferroelectric crystals for photonic applications, and laboratory-on-a-chip for biomedical applications. He was an Elected Fellow of SPIE, in 2008, and a fellow of the Optical Society of America, in 2010. In 2020, he was the recipient of the SPIE Dennis Gabor Award